AI-Based Supervision for a Stirred Extraction Column Assisted with Population Balance-Based Simulation

Laura Neuendorf, Zakariae Hammal, Armin Fricke, and Norbert Kockmann*

DOI: 10.1002/cite.202200241

Solvent extraction as environmental benign separation technique can be modeled in physical detail by population balance of the droplet size distribution. However, much information on the droplet generation and coalescence is necessary for representative results. In this contribution, we present a comparison of AI-evaluated experimental and simulated data on the behavior of a stirred solvent extraction column with an inner diameter of 32 mm. Lab experiments were performed using the standard test system with *n*-butyl acetate, acetone, and deionized water. A digital camera is placed in front of the middle section as well as the head of the column. Droplet size evaluation is performed using a retrained neural net (Mask R-CNN). The stirred DN32 extraction column is modeled and simulated using a 1D CFD population balance software. The simulation allows for behavior analysis, trends comparison, and validation of the hydrodynamics and mass transfer performances.

Keywords: Liquid-liquid extraction, Mask R-CNN, Population balance modeling, Process simulator, Solvent extraction

Received: December 20, 2022; *accepted:* April 11, 2023

1 Introduction

For the time being, energy supply becomes a primary concern for governments, industrial practitioners, and end consumers [1, 2]. The current energy supply situation calls for short-, medium- and long-term actions that should be taken to reduce the costs starting from energy-savings practices, process energy optimization to new technology developments that rely on low energy demand. Particularly, in the chemical industry, separation processes have a non-negligible share of the energy consumption [3, 4]. Liquid-liquid extraction is gaining interest and application due to its operation at low-energy cost. The exploration and synthesis of new solvents make the liquid-liquid extraction unit more promising to use. Furthermore, liquid-liquid extraction finds wide applications in the field of bio-product separation at low operating temperatures to avoid degradation of temperature-sensitive products. [5, 6]

The operation of the solvent extraction process is better improved with process supervision and control [7]. With additional supervision, more insights into the hydrodynamics of the process are generated [8]. There are many examples where additional process supervision enables a more precise process tuning due to the additional availability of data. For example, the supervision of flow patterns in bioreactors enables a more precise O_2 input rate into the process. Or a crystal size distribution monitoring enables for setting more precise temperature profiles in solids handling processes [9–11]. For visual process monitoring, an optical sensor is necessary. Here, a digital camera is placed in front of the solvent extraction column and continuously takes images of the process and evaluates it using computer vision. A further development of computer vision lies in the use of artificial intelligence (AI)-based methods. They are increasingly used in supervising processes, as the equipment is low cost and robust. [12–14]

The aim of the additional supervision lies in the refined process control. However, to completely scan the operating window a lot of chemicals are consumed. Therefore, simulation should assist the above-described approach to reduce the number of experimental tests, for data generation, the use of the chemical liquids and energy consumption for their recovery. Simulation supports decision making, while comparing the experimental data to simulation results confirming the accuracy of the measurement procedures. However, the model used in simulation should be reliable for its

[1]Laura Neuendorf https://orcid.org/0000-0001-6593-1752,
[2]Zakariae Hammal, [2]Prof. Dr. Armin Fricke,
[1]Prof. Dr.-Ing. Norbert Kockmann
(Norbert.kockmann@tu-dortmund.de)
[1]TU Dortmund University, Department of Biochemical and Chemical engineering, Laboratory of Equipment Design, Emil-Figge-Straße 68, 44227 Dortmund, Germany.
[2]CGC Capital-Gain Consultants GmbH, 10117 Berlin, Germany.

prediction, by capturing significant phenomena and showing flexibility to fit relevant model parameters as it was reported in [15]. We used PPBDesigner, a population balance-based column module integrated in the DWSIM Pro process simulator to simulate discrete flow systems such as solvent extraction columns. This contribution describes the theory behind the population balance equation and the experimental approach to determine the specific parameters. Finally, simulation setup and results of the column with two different operating conditions are provided to compare the experimental data with the data generated from simulation.

2 Theory

2.1 Solvent Extraction

The effectiveness in separation processes can be generally improved by using multiple contacting stages, with each stage approaching equilibrium, in a cascade and/or by using a sequence of two or more different types of separation methods in a hybrid system [16]. Countercurrent liquid-liquid extraction uses multiple contacting stages. In countercurrent liquid-liquid extraction columns, ideal plug flow is the desired flow pattern as it results in maximum concentration gradients between the phases, leading to high mass transfer rates [17, 18]. Moreover, the larger the interfacial area between the two liquid phases, the better the substance transfer of the value component from the first, usually aqueous to the second, usually organic phase. However, the larger the interfacial area, the smaller the resulting droplets in the column are. Yet, too small droplets lack of buoyancy force, leading to a worse separation efficiency over time, since the droplets remain in the column for too long time. An optimum in the size of droplets can be determined for a given substance system that balances the effect of a large desired interfacial area and droplets that still show sufficient buoyancy to leave the column.

2.2 Deep Learning Using Mask R-CNN

Deep learning (DL) algorithms are designed to mimic the function of the human cerebral cortex. They are representations of deep neural networks, i.e., neural networks with more than one, often many hidden layers. Because DL models have many layers, the abstraction capacity is especially high. The early layers learn abstract, basic shapes such as edges or curves, while the later layers learn more complex geometries. Thus, a DL model can generate abstractions of the input data on different levels, which can be used to solve the machine learning problem – also referred as "mapping from features" or "classification" – more efficiently. A (deep) neural net can thus be imagined as an add-on before a machine learning classifier. Convolutional neural networks (CNNs) are deep learning algorithms that can train with large datasets consisting of millions of parameters. CNNs are designed especially for image recognition tasks. This is because they consider the spatial arrangement of information, and they convolve it with filters to produce the desired outputs. [19, 20]

For image analysis tasks, there are several options: whole images might be classified, an object within an image might be located or single pixels are assigned so several objects within one image, which is called instance segmentation. In this work, instance segmentation is used to exactly locate the droplets in the image. This way, quantitative information about the size of the drops can be accessed directly out of the segmented image. [20]

When using deep learning, a network can be built "from scratch", where a decision about how many layers of which kind, and how many nodes per layer for each layer must be made. The created architecture must be tested, if it is a good compilation or not, and eventually the net must be redesigned. Or instead, transfer learning can be used, which makes use of already existing nets. A trained net is retrained to adapt to new data. Therefore, the trained weights of the convolutional and fully connected layers are reset. Training is further explained in the next section.

Transfer learning is carried out in this work, because it is time-saving compared to the design of a new network and provides a tried and tested network architecture, with a beneficial composition of layers consisting of a suitable number of nodes. Here, Mask R-CNN is used as a convolutional neural net, its structure can be seen in Fig. 1.

Mask R-CNN stands for regional convolutional neural network and consists of a framework that can be divided into two stages. The first stage is characterized by that the R in the name: the region proposal network (RPN). In this first stage, the image is fed into a CNN, which has the purpose of identifying regions of interest (ROI) and to feed them to the next stage. The second stage consists of the classification of the individual ROIs and the generation of the bounding box for the recognized objects and finally the generation of the pixel-precise masks. [22]

The first stage consists of three components in general. The basic framework is the ResNet-50 in combination with a so-called feature pyramid network (FPN) and the subsequent RPN. With the help of the early convolutional (CONV) layers, low-level features are detected first, and successively higher-level features are detected with higher layers. This forms an initial pyramid of layers.

The FPN, as the name suggests, forms another pyramid of layers. In these layers, the higher-level features are fed from the CONV layers and passed back to the lower CONV layers. This leads to the fact that the CONV layers have access to both higher-level and lower-level features. The final component of the first level is the RPN. The RPN glides over the input image, establishing regions of fundamental interest based on the features detected in the ResNet + FPN by using the presence of features as a criterion in a class-

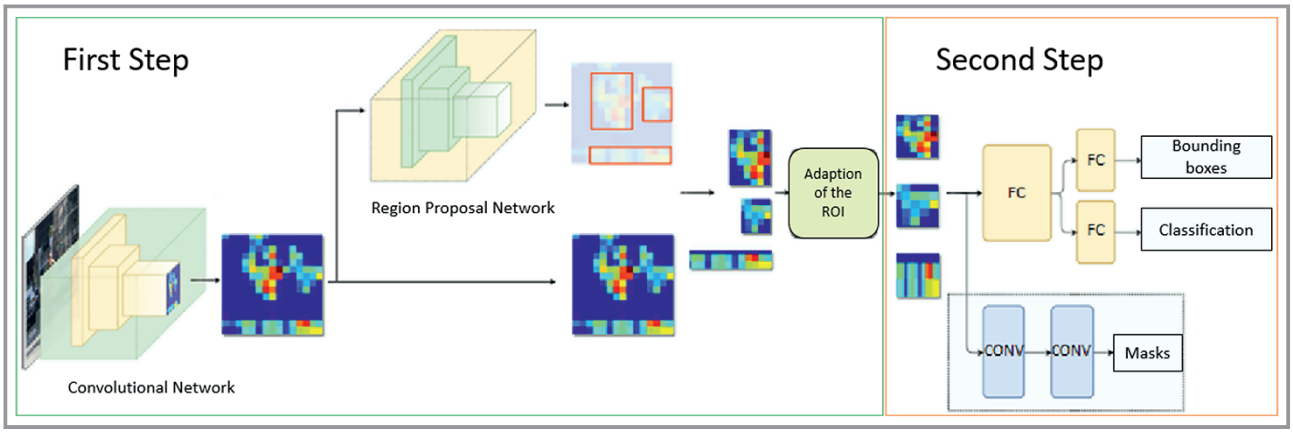

Figure 1. Architecture of the M-RCNN. First, the features are extracted by a CNN based on ResNet-50 and an FPN. These features are then detected and selected using a region proposal network (RPN). The selected regions of interest ROIs (anchors) are converted to a uniform format (green, first stage). Subsequently fully connected (FC) layers are used to generate the bounding boxes and classification. Via convolutional (CONV) layers the masks are generated (orange, second stage). Adapted from [21, 22].

independent manner. The resulting regions are realized in the form of rectangular boxes called anchors and vary in both size and aspect ratios. Furthermore, the anchors can also overlap to cover as much of the image as possible. In RPN, the anchors are then used to produce two outputs; a classification of whether it is likely to be a foreground or background object within the anchor, and for the foreground anchors, a correction vector, which readjusts the anchor that may not fit perfectly. This foreground anchor is the result of a selection of all anchors which overlap strongly, the anchor that has the highest chance to contain the object. [23]

The anchors generated in the first stage are used in the second stage for two different process pipelines. A bounding box and classification are performed for each anchor passed. This is done by a deeper interconnection of CONV layers for feature extraction with pooling layers and FC layers. It is therefore very similar to the procedure in stage one, but the network is much deeper and can now assign a final class to the objects. Classifications, however, require constant input dimensions of the data for reliable detection. Because the anchors vary in size, the features of the anchors are cropped and scaled to identical dimensions before being passed on to the CONV layers. Classification can also result in assignment to the background class, which causes the anchor to be discarded. Likewise, the dimensions and position of the anchor are refined and finally output as a bounding box. [23, 24]

The second process pipeline is used to output the mask of an object within the anchor. The anchors declared as foreground are fed into a CNN, which generates so-called soft masks with a size of 28×28 pixels. These soft masks contain a floating-point number in each pixel, which preserves the information density. The masks are resized in the last step to be scaled up to the size of the corresponding bounding box and converted into a binary mask. Thus, a single final pixel-precise mask is generated per object. [23]

2.3 Modeling Using Population Balance Equation

The population balance model combines the hydrodynamic and mass transfer phenomena in liquid-liquid extraction (LLE) columns. It describes the evolution of a particle or a droplet size distribution of a dispersed phase (single particles or particles in swarm) in a continuous phase. The model gives a realistic description of the behavior of the discrete phase by considering breakage and coalescence phenomena, axial dispersion, and buoyancy-driven motion of drops inside the LLE column, where most of these phenomena are lost in the classical models (back-mixing and dispersion models).

The general population balance equation describing the coupled mass transfer and hydrodynamics in LLE columns in a one-dimensional domain is expressed as [25]:

$$\frac{\partial \mathrm{n_{d,cy}}(\psi)}{\partial \mathrm{t}} = -\frac{\partial\left[\mathrm{u_y n_{d,cy}}(\psi)\right]}{\partial \mathrm{z}} + \frac{\partial}{\partial \mathrm{z}}\left[\mathrm{D_y}\frac{\partial \mathrm{n_{d,cy}}(\psi)}{\partial \mathrm{z}}\right] - \sum_{\mathrm{i}=1}^{2}\frac{\partial\left[\dot{\xi}_{\mathrm{i}}\mathrm{n_{d,cy}}(\psi)\right]}{\partial \xi_{\mathrm{i}}} + \frac{\mathrm{Q_y^{in}}}{\mathrm{A_c}}\mathrm{n_y^{in}}(\mathrm{d},\mathrm{c_y};\mathrm{t})\delta(\mathrm{z}-\mathrm{z_y}) + \gamma(\psi) \quad (1)$$

The vector $\psi = [d, c_y, z, t]$ is composed by the droplet internal coordinates (diameter d and solute concentration c_y), and the external coordinate (column height z and the time t). The velocity vector along the internal coordinates is given by $\dot{\xi}_i = \left[\dot{d}, \dot{c}_y\right]$. Here, u_y is the droplet rising velocity and D_y is the dispersed phase axial dispersion coefficient.

The state of any droplet is given by a bivariate density function $n_{d,cy}(d,cy;z,t)$, where $n_{d,cy}[d,c_y,z,t]\partial\mathrm{d}\partial\mathrm{cy}$ denotes the number of droplets having droplet size and solute concentration in the range $[d, d + \partial d]$ and $[c_y, c_y + \partial c_y]$ per unit volume of the contactor. The parameter $\gamma(\Psi)$ is a source term that accounts for the net number of droplets produced by breakage and coalescence.

$$\gamma(\psi) = B^b(\psi) - D^b(\psi) + B^c(\psi) - D^c(\psi) \quad (2)$$

The equation describes four rates due to the birth (B) and dead of drops (D) caused by breakage (b) and coalescence (c) mechanisms. A detailed presentation of the source term can be found in Attarakih et al. [25].

2.3.1 Droplet-droplet interaction models

Breakage

Many factors affect the breakage mechanism including droplet size, viscosity of the system, density, energy dissipation, and volume fractions of both continuous and dispersed phase. If the energy of a turbulent eddy exceeds a critical value, the droplets interface becomes unstable, and it breaks up. The column's type and internals have high effect on the breakage of droplets especially in agitated extractors.

In recent development, breakage frequency of single droplets is expressed as function of the modified Weber number We_{mod}, which can be found in the work of Bahmanyar and Slater [26] and Cauwenberg et al. [27]. The latter modified the Weber number to include the effect of critical rotor speed and the effective interfacial tension [27]:

$$We_{mod} = \frac{\rho_x^{0.8}\eta_x^{0.2} d\, D_R^{1.6}(2\pi)^{1.8}\left(N^{1.8} - N_{crit}^{1.8}\right)}{\sigma} \tag{3}$$

The above equation describes the ratio of the destructive forces of the flow in the compartment to the stabilizing forces from the interfacial tension. The parameter N_{crit} is the critical rotor speed, below which the breakage probability falls to zero. Many correlations are developed for agitated columns based on the modified Weber number and different critical rotor speed expressions and can be found in the literature [28–30].

Coalescence

Drop coalescence is another important phenomenon that should be well described in the PPB model. Studies have shown that drops coalescence has direct dependency on the properties of the chemical system used, droplet size, and hydrodynamics inside the column [31]. The coalescence term has one single parameter to be defined, which is the coalescence rate $\omega\left(d, d', \emptyset_y\right)$. Many authors proposed phenomenological models to describe the coalescence rate which are based on the collision frequency and coalescence efficiency concepts [32–34]:

$$\omega(d, d') = h(d, d')\lambda(d, d') \tag{4}$$

The coalescence frequency $h(d,d')$ of two droplets is described by Coulaloglou and Tavlarides in analogy to collision frequency between two gas molecules [35]. The coalescence efficiency $\lambda(d,d')$ describes the contact time between two droplets and time of their coalescence. PPBDesigner include the above correlation to estimate the coalescence rate. However, the correlation has two adjustable parameters that need to be fitted using experimental data. For some known column types, geometry and the chemical system, the adjustable parameters are given in literature [36–38].

2.4 Droplet Velocity

The rise velocity of dispersed phase is function of droplet relative velocity and the velocity of the continuous phase. For countercurrent flow, it is expressed as:

$$u_y\left(d, \emptyset_y\right) = u_r\left(d, \phi_y\right) - u_x \tag{5}$$

The droplet relative velocity is given by:

$$u_r\left(d, P, \emptyset_y\right) = u_t\, K_v(d)\left(1 - \emptyset_y\right)^m \tag{6}$$

where $\emptyset_y$ is the dispersed phase holdup and P represents dependency on system chemical and physical properties. Concerning the terminal droplet velocity u_t, many correlations are developed depending on the chemical system and the droplet behavior [39–42].

The parameter $K_v(d)$is a slowing factor considering the effect of the droplet diameter and the column internal geometry on the velocity of the dispersed phase $0 < K_v < 1$. Correlations are available to estimate the slowing factor and recent ones are embedded in PPBDesigner. The exponent m is a function of the particle Reynolds number, which indicates the degree of swarm influence. More detailed description of the exponent m can be found in Godfrey et al. [43]

3 Materials and Methods

3.1 Experimental Setup of the Extraction Column

The creation of the image dataset is carried out using a DN32 stirred extraction column made from glass with an inner diameter of 31.3 mm and an active extraction height of 400 mm consisting of 20 compartments. The aqueous, heavy feed phase is the continuous phase (indicated by yellow arrows in Fig. 2.) and leaves the column as the raffinate. The discontinuous, light phase is the organic, discontinuous phase and leaves the column as extract at the top (indicated by orange arrows in Fig. 2.).

The height of a compartment (seen on the left side in Fig. 2) is 20 mm each and includes a six-blade stirrer with a height of 5 mm. All stirrers are mounted on a central shaft [44]. The shaft is rotated by a Heidolph RZR 2102 control stirrer drive (Heidolph Instruments GmbH & Co. KG, Schwabach, Germany), which ensures the intense mixing of the phases. Further geometric information on the internals is given in Tab. 1 in Sect. 3.3.1, as it is needed for the simulation. The continuous, aqueous phase is fed from a vessel into the top part of the column by an Ismatec masterflex 5202FD (peristaltic or gear) pump (Cole-Parmer GmbH, Wertheim, Germany). At the column's bottom, the continu-

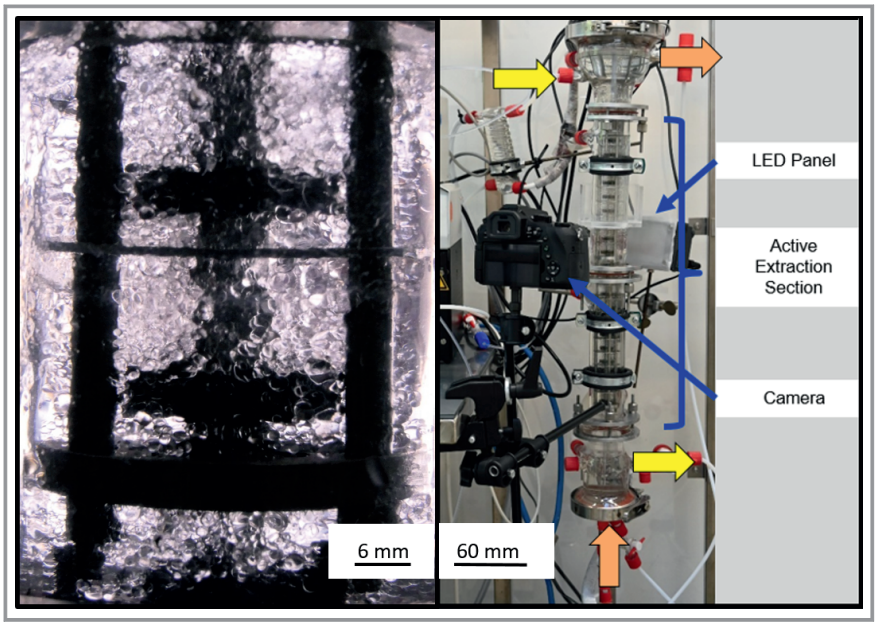

Figure 2. Experimental setup of the solvent extraction column. Left side: close-up view of a single compartment, bordered by an upper and lower sieve plate. Right side shows the position of the digital camera, the LED panel and the active extraction section as well as the solvent inflow and exits.

ous phase leaves the column and is conveyed out by an Ismatec REGLO-Z gear pump. The pump is adjusted in that way that the interface between the two immiscible phases at the top of the column remains at a constant level between two level sensors, preventing the heavy continuous phase from leaving the column via the outlet at the top. At this raffinate outlet, a three-way valve, where a sampler can be connected to, is located. At the same time, the Lenze D-32696 pump (Lenze SE, Aerzen, Germany) conveys the disperse phase into the column through a glass cannula at the bottom. Furthermore, chemically resistant fluorinated ethylene propylene (FEP) tubes are used for connecting pumps and equipment. All flange connections are sealed with silicone. The digital Nikon Z6 camera with an image resolution of 180 dpi is kept in a constant position by a tripod. The central, 11th and 12th compartment are monitored with a set frame rate of seven images per second. A light-emitting diode panel ensures constant backlighting for constant image contrast.

A two-component liquid-liquid system is used for hydrodynamic characterization. As discontinuous, organic phase, *n*-butyl acetate (99.5 % purity, Merck KGaA, Germany) and as heavy, aqueous phase deionized water was used is used in all experiments. The aqueous phase mass flow rate is kept constant at 30 mL min^{-1} and the organic flow rate is varied from 15 to 44 mL min^{-1}. A three-component liquid-liquid system is used for substance transfer investigations with 5 wt % acetone (99.5 % purity, VWR Chemicals, Germany) added to the aqueous phase. The acetone concentration in the raffinate is measured by putting the sampler into a self-build, customized ultra-violet-(UV) spectroscopy sensor based on Arduino, adapted to UV-spectra after [45].

3.2 Image Evaluation Using a CNN

Process supervision enables a more precise process control. Therefore, an instance segmentation algorithm using CNNs is developed. The CNN algorithm detects the size of droplets in the column. At first, the network must be trained for this task, thus an image data set has to be created as the first step. Here, 150 images showing different operating conditions are taken at various stirrer speeds and different load states. In every image 30–40 accurately visible droplets are labeled in VGG image annotator (VIA) using polygons. The manually labeled image data set is split into an 80/20 % ratio for the training and a validation data set.

To obtain information about incorrectly classified objects in images accuracy as a metric is applicable. Here, the terms true positives t_p, where positive cases are correctly identified as positive and true negatives t_n, where negative cases are correctly identified as negative are introduced. Furthermore, false positives f_p, where negative cases are falsely identified as positive, and false negatives f_n, where positive cases are falsely identified as negative need to be introduced. Then accuracy is defined as [46–48]:

$$Accuracy = \frac{t_p + t_n}{t_p + t_n + f_p + f_n} \tag{7}$$

The ideal training duration was found to be 500 iterations. After finishing the iteration step, Mask R-CNN achieves the highest final training accuracy as a plateau of 88 % approximately. Furthermore, 1000 and 20 000 training iterations were tested, too, the model then detects drops with higher confidence, but the number of detected droplets is significantly lower. The reason is probably an overfitting of the model to the training data.

Another applied metric is the intersection over union (IOU), also named Jaccard-Index, which describes the ratio of correctly classified pixels to the total number of ground truth and predicted pixels in that class. It thus describes the detection confidence that Mask R-CNN assigns to every droplet it detects in an image.

$$IOU = \frac{t_p}{t_p + f_p + f_n} \tag{8}$$

As not all visible droplets were manually labeled, accuracy might deteriorate due to the detection of some false

positives. Since false positives are most likely also correctly detected droplets, their detection is not so bad and therefore Mask R-CNNs detection confidence threshold (IOU) should be set low. By varying the threshold, from values of 0.1, 0.25, 0.4 and 0.7 detection performance was tested on 12 test images.

Here it was found that a value of 0.1 is too low and produces unreasonable false detections, where, e.g., the sieve plate was detected as a droplet (cf. Fig. 3, left image). A detection confidence from 0.4 or higher only leads to a lesser number of detected droplets (cf. Fig. 3, right image). Therefore, the final detection confidence threshold was set to 0.25 (cf. Figure 3, central image). After training the CNN to this task, the droplet size within the column during operation is evaluated. Therefore, an image preprocessing routine follows, where the desired image section is cut out as indicated in Fig. 3.

3.3 Simulation Using PPBDesigner

3.3.1 PPBDesigner Column Module

PPBDesigner is software for modeling and simulation of discrete flow systems, such as liquid-liquid extraction columns with an application of detailed population balances. It uses modern population balance solvers to discretize the internal particle coordinates, while the built-in space-time solvers are utilized to discretize the temporal-spatial domain. PPBDesigner is a built-in column module in DWSIM Pro, the commercial sibling of the open-source process simulator DWSIM. For this study we have used DWSIM Pro version 8.2.0 and PPBDesigner version 1.3.0.

The DWSIM Pro tool PPBDesigner is developed to model and simulate discrete flow systems, and in particular liquid-liquid extraction columns, using detailed population balances. It is embedded in DWSIM-Pro process simulator as a package of unit operations and allows the integration with other rigorous unit operations for a complete process flow diagram simulation. The PPBDesigner algorithm is composed of the population balance equation (PBE) solver with a discretization of the internal coordinates (drop diameter and concentration) and the space solver with a discretization of the spatial domain. The PBE solver uses advanced numerical methods like the quadratic method of moments (QMOM) and extended fixed pivot method (EFPMT).

Figure 3. Results of Mask R-CNNs droplet detection for different confidence thresholds, left side IOU = 0.1, central image IOU = 0.25, right side IOU = 0.4 set as threshold.

3.3.2 User Interface and Inputs

PPBDesigner has an editor to setup all the input parameters to model and simulate an LLE column. Tab. 1 shows all input parameters that are required. By default, PPBDesigner editor is displayed in a standard mode, where important but not necessary parameters are hidden for a simple simulation environment. The user has to enter inlet experimental data and column dimensions to correctly setup the simulation.

Table 1. Input tabs in PPBDesigner editor.

Tab	Type of input
Internal/external column geometry	User
Operating conditions	User
Mass transfer and axial dispersion coefficients	Correlations
Column hydrodynamics (breakage/coalescence)	Correlations
Inlet drop diameter and distribution	User
Distribution coefficient	User value or correlation
Solver settings	Default or user

3.3.3 Simulation of the Lab-scale Stirred Column

The lab-scale stirred column of Kühni type shown in Fig. 2 is simulated with PPBDesigner in the DWSIM Pro flowsheeting environment. Internal dimensions of the stirred column are needed to predict the hydrodynamics in the column module, see Tab. 2.

Inlet heavy and light phase compartment, the inlet mean diameter of drops, and other specifications are also determined based on the experimental setup. To fit the adjusted parameters of the coalescence model, a first set of measured drop size data at different rotational speed is used. For further simulations, the adjusted parameters are kept constant. The simulated column is shown in Fig. 4.

Mass transfer and axial dispersion coefficients of both phases

Table 2. External and internal dimensions of the DN32 extraction column [44].

Parameter	Value
Column diameter [mm]	31.3
Compartment height [mm]	20
Number of compartments [–]	20
Stirrer diameter [mm]	18
Exchange surface area [mm^2]	769
Plate diameter [mm]	31.3

are selected from the available database in PPBDesigner. The velocity model of the dispersed phase is selected based on the analysis of the behavior of the chemical system used and observations from the experimental work.

Hydrodynamic and mass transfer results are displayed numerically in the flowsheet environment. Graphical visualization of the results (e.g., holdup profile, diameter profile, solute transfer profile, ...) can be seen in separate tabs within the software. Mass transfer and hydrodynamic performances are presented as function of the column height.

4 Results

4.1 Results of Experimental Droplet Size Estimation

The resulting average droplet size of the system is calculated to see if the current settings provide optimal hydrodynamics of the extraction column. In the column, previous work showed an average droplet size of 1 mm to be the hydrodynamically preferred operating state [46]. Results of this investigation of 50 images per operating condition are shown in Fig. 5.

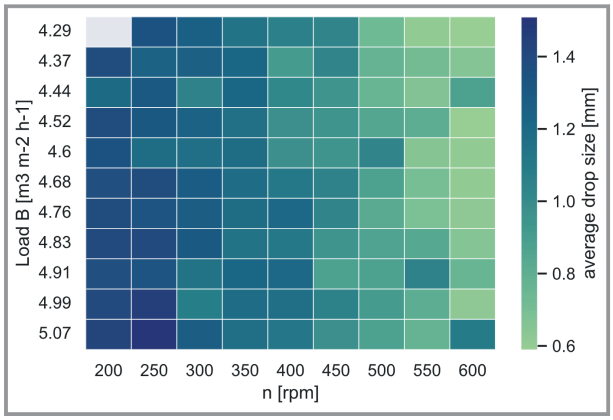

Figure 5. Determined average droplet size of droplets in the butyl acetate/deionized water system in the stirred extraction column as a function of their load *B* and the stirrer speed *n*.

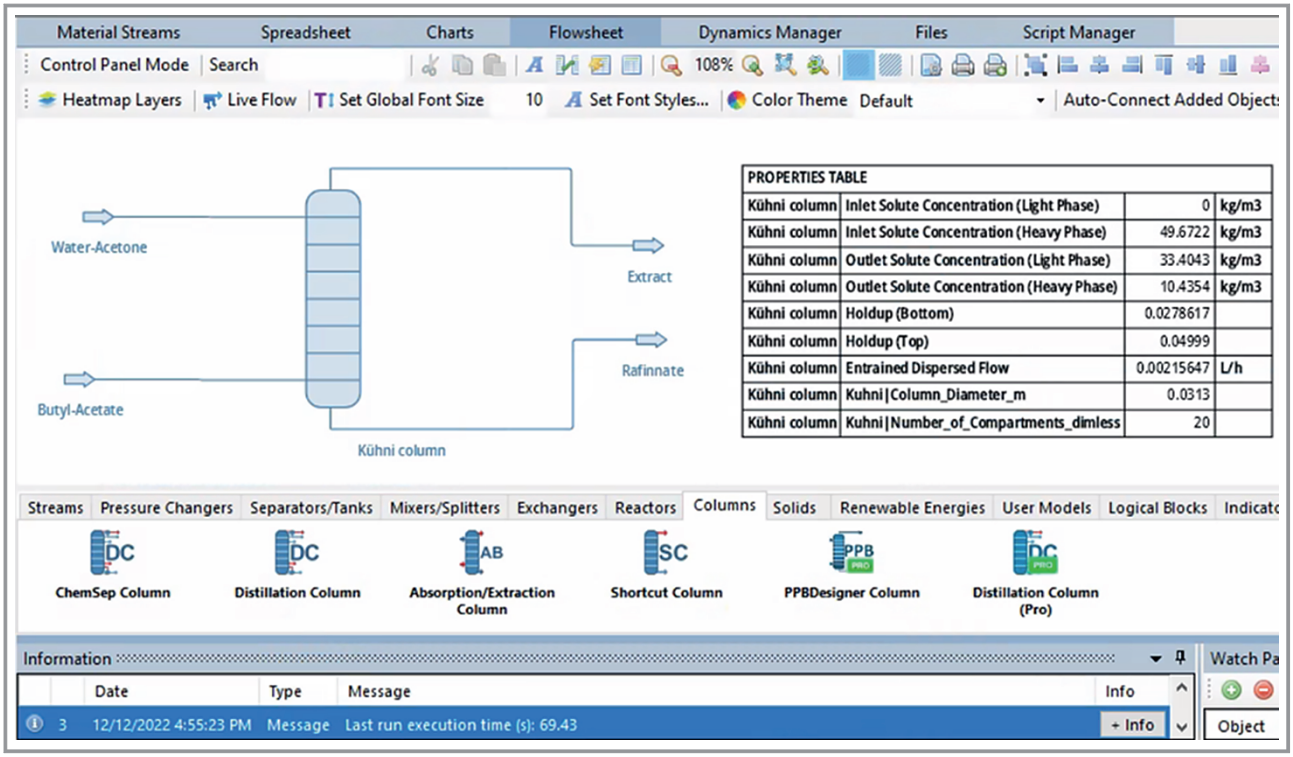

Figure 4. Simulation of the stirred column with basic results displayed in the flowsheet environment.

It can be seen that the droplet size for the system ranges from 0.6 to 1.5 mm in the operating range. Approx. ± 0.2 mm deviations occur during estimation of the average sizen due to natural fluctuations of such a dynamic system. At various loads and stirrer speeds, the favored operating condition of approx. 1 mm average droplet size can be seen in the range of 350–400 rpm [46]. Furthermore, it can be seen that the stirrer speed has a stronger influence on the droplet size than the loading B of the column. This is to be expected due to the high mechanical energy input.

4.2 Results of Mass Transfer Investigation

For mass transfer investigations in LLE, a crucial parameter is the time until a steady-state operation is reached. This was investigated for the *n*-butyl acetate/deionized water system in the stirred extraction column with an aqueous phase volume flow rate of 30 mL min^{-1} and a solvent volume flow rate 18 mL min^{-1} (see Fig. 6).

Measurements were started 45 min after the begin of the column operation as no stationary operation was expected before that time. As one can see, the steady state is reached about 90 min after the start of the operation. This means 2.7 L of *n*-butylacetate have been used to determine the steady state of one single operating point. Therefore, substance transfer measurements are time consuming and the consumption of chemicals is high.

4.3 Simulation Results and Comparison

The high time effort and chemical consumption was the reason to investigate, whether simulation can also lead to comparable results to gain knowledge about the column operation faster. Experiments were performed using the minimum amount of chemicals. The aqueous phase volume flow rate of 15 mL min^{-1} and a solvent volume flow rate of 18 and 20 mL min^{-1} are used to separate the acetone from deionized water.

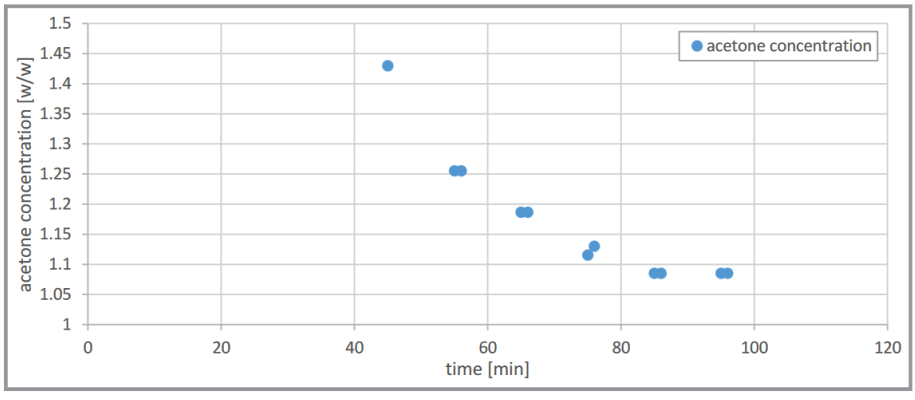

Figure 6. Determined acetone concentration over time in the butyl acetate/deionized water system in the stirred extraction column with an aqueous phase volume flow rate of 30 mL min^{-1} and a solvent volume flow rate of 18 mL min^{-1}.

4.3.1 Drop Size Estimation

The obtained drop sizes of the experiments observed with Mask R-CNN and PPBDesigner are plotted in Fig. 7. Simulation results show a good agreement with the corresponding experimental data. Except for the first point in the left diagram at low stirrer speed (300 rpms). Here the deviation between experiment (1.48 mm) and simulation (1.2 mm) is 23 %. It was observed in the experiment that, at low stirrer speed, drop diameter range is from 0.20 mm to 0.25 mm. The deviation is within this range. Furthermore, because of the small column dimensions, drops retention beneath the stator is usually higher. In fact, the stirred lab-scale column has a perforated stator plate instead of a stator with one hole opening (cf. [44] for a detailed technical drawing). The design of the perforated plate hinders the motion of drops with big size at low stirrer speed, causing more coalescence of drops. This dispersion effect is captured by the axial dispersion coefficient correlation, which is a function of drop size and drop velocity, but at small column dimensions and low stirrer speed, the axial dispersion is neglected in the population balance equation [42]. Measurement points with higher stirrer speed lie very close to their respective simulation results. This indicates that the model can catch all the dominant phenomena in the lab-scale column. On the other hand, with an S/F ratio of 1.2 and for 600 rpm, the experimental data indicate a lower drop size (0.62 mm) than the simulation suggests (0.70 mm). This deviation of 11 % indicates that the hydrodynamic model predicts well the experimental data as the average reported error in literature is 15 % [49].

On the other hand, when the S/F ratio is 1.33, the drop size at 600 rpm shows a much better congruence between the results. Here, only 300 rpm just as in the left diagram stands out with 19 % deviation. Again, this might be since the predominance of coalescence phenomena in the lab-scale column is higher than anticipated by the model.

4.3.2 Mass Transfer Performance

Solute transfer from the heavy continuous phase to the light dispersed phase is simulated and compared to the solute measurement at the raffinate stream. Mass transfer performance of the column is shown at two different operating conditions with an S/F ratio of 1.2 at the left side and S/F ratio of 1.33 at the right side of Fig. 8.

The simulation results in both scenarios are in a good agreement with the corresponding measure-

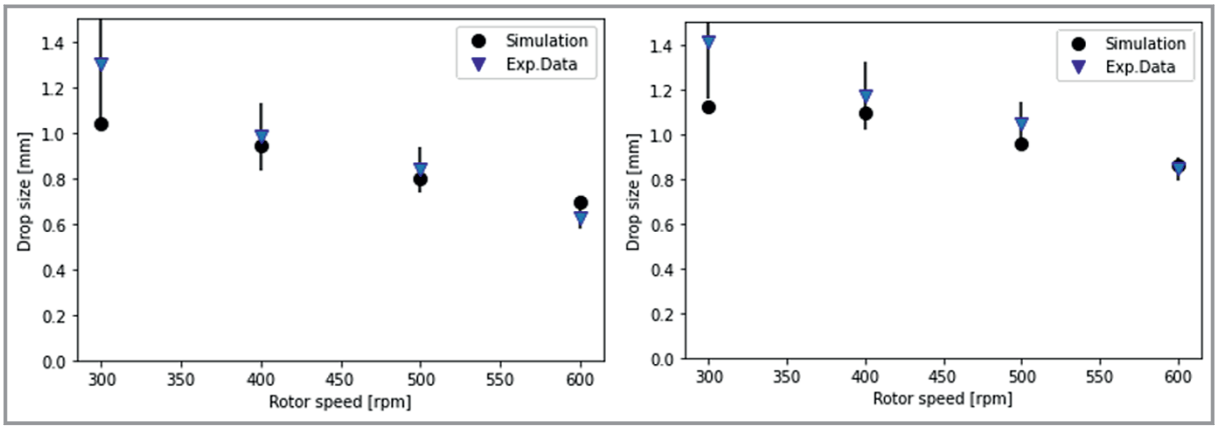

Figure 7. Drop size change at different stirrer speed and solvent-to-feed (S/F) ratios. Left side S/F ratio = 1.2, right side S/F ratio = 1.33.

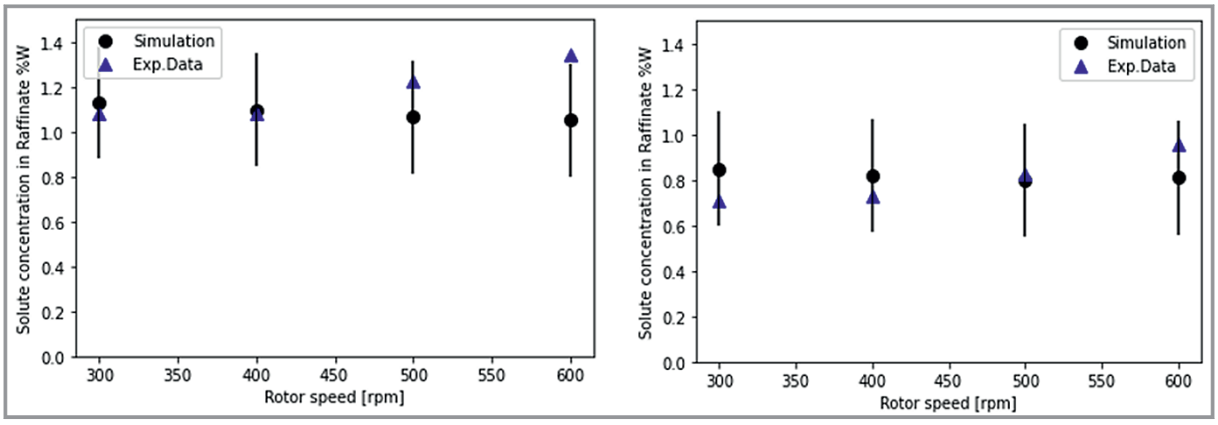

Figure 8. Solute transfer performance at different stirrer speed and with an S/F ratio of 1.2 at the left side and S/F ratio of 1.33 at the right side. Error bars of the simulation set to 20 %.

ment data for lower stirrer speeds of up to 500 rpm. The deviation rises with the increasing stirrer speed. At high stirrer speed (600 rpm) the simulation results show a higher deviation. The error bar is set to 20 %, which is the common error value reported in literature [49]. At 500 and 600 rpm the *n*-butyl acetate droplets are rather small with an average size of 0.6 mm in diameter. PPBDesigner detected some entrainment of solvent droplets within the continuous phase, which indicates that the separation efficiency of the column is decreasing under these conditions. As droplets circulate a very long time in the same column compartment and entrained with the continuous phase, *n*-butyl acetate droplets rich of acetone exhibit inverse transfer from the organic to the aqueous phase resulting in higher concentration at the raffinate stream. However, it is not yet confirmed if entrainment is detected in the lab.

The mean average drop size is also investigated. The comparison between experimental data and simulation results shows a disagreement at low stirrer speed for both scenarios, see Figure 7. The disagreement is due to the estimation of the energy input in the simulation. In fact, the breakage frequency strongly depends on the energy input of the stirred columns as illustrated in the modified Weber number, see Equation (3). Different correlations are developed to estimate the critical rotor speed, at which the breakage probability falls to zero. At low stirrer speed, the correlation used shows a limitation in predicting the breakage frequency and, therefore, the average drop size of the studied chemical system. In general, simulation results are in good agreement with the corresponding experimental data with a maximum deviation close to the 20 % accepted error margin reported in the literature. The model predicts reasonably well hydrodynamic and mass transfer performances of the lab-scale stirred column at different operating conditions. The fitted coalescence parameters are kept fixed in all simulation scenarios along with other correlations for drops velocity, mass transfer coefficients and axial dispersion. Therefore, the simulation can assist this work with reliable simulation data especially in the middle of the given operating window without relying much on the experimental work.

Simulation and results, as well as previous work indicate an operation optimum at a stirrer speed of around 350–400 rpm, here the least amount of acetone in the raffinate is expected and detected. This correlates to a desired average droplet size of 1 mm (cf. Fig. 5 and 7) [44, 46].

5 Conclusion & Outlook

We used CNN-based supervision of the hydrodynamic performance of a stirred DN32 liquid-liquid extraction column. We succeeded in training a neural network on image analysis for the instance segmentation of droplets, even though they are partly overlapping. For the investigated chemical system of *n*-butyl acetate and water, the optical supervision of the droplet size leads to the conclusion that with stirrer speeds up to 300 rpm the generated droplets in column are too large and thus the interfacial area is too small. Here, a reasonable countermeasure is increasing the stirrer speed. On the other side, too small droplets form with a stirrer speed of 500 rpm and higher, where the stirrer speed is reduced stepwise until medium-sized drops are obtained.

The ideal stirrer speed is between 350–400 rpm for all investigated loads (cf. Fig. 5) and S/F ratios (cf. Fig. 7 and 8). The operation optimum is also confirmed by simulation. The simulation results show a fair agreement with the corresponding experimental data. Higher deviation of 19 % in the estimation of the drop size at low stirrer speed is seen. Mass transfer performance shows a deviation of 20 % of the results from the experimental data. Different phenomena that occur inside the extraction column can explain the deviations found since they are not captured yet by the population balance model, like the impurity effect, Marangoni effect, and swarm effect.

As an outlook, using simulation to generate additional training data for a following control concept based on a reinforcement learning algorithm seems feasible as the amount of experiments in the laboratory might be reduced and thus time, energy and chemicals will be saved.

Moreover, pulsation should be integrated into the column to further increase holdup of the dispersed phase with higher separation performance and thus its potential for process intensification with solvent extraction [23]. Also, first investigations indicate a reduction of time to achieve steady-state operation compared to the 90 min without pulsation (Fig. 6).

As a further outlook, pulsed columns have also many applications, especially because of their non-mobile internals, which reduces maintenance cost compared to agitated columns, ease of operation, and robustness. This column type is also to be modeled and simulated using the population balance framework and added to the PPBDesigner suite of different extraction column types.

Acknowledgment

The BMWK is acknowledged for funding this KEEN project initiative (Support code: 01MK20014S, 01MK20014E). The authors want to thank Carsten Schrömges and the glass manufacturing workshop. The authors want to thank Prof. Dr.-Ing. Menwer Attarakih, Professor at the University of Jordan, Amman, for his contribution in developing the PPB Designer tool. Open access funding enabled and organized by Projekt DEAL.

Symbols used

B_c	[ms^{-1}]	Birth of droplets by coalescence
B_d	[ms^{-1}]	Birth of droplets by breakage
c_x, c_y	[kg m^{-3}]	Solute concentration: continuous phase, dispersed phase
d	[m]	Droplet diameter
D^b	[ms^{-1}]	Dead of droplets by breakage
D_R	[m]	Rotor diameter
D^c	[ms^{-1}]	Dead of droplets by coalescence
$h(d,d')$	[m^{3}s^{-1}]	Coalescence frequency
K_v	[–]	Slowing factor
m	[–]	Swarm exponent
$n_{d,cy}[d\ cy;\ t\ z]$	[m^{-3}]	Bivariate density function of droplets
N	[s^{-1}]	Agitator speed
N_{crit}	[s^{-1}]	Critical rotor speed
$P(d)$	[–]	Breakage probability of droplet with diameter d
u_{char}	[m s^{-1}]	Characteristic velocity
u_r	[m s^{-1}]	Relative velocity
u_x	[m s^{-1}]	Continuous phase velocity
u_y	[m s^{-1}]	Velocity of dispersed phase
U_t	[m s^{-1}]	Terminal velocity

Greek letters

$\Gamma(d', \emptyset_{\mathbf{y}}, P)$	[s^{-1}]	Breakage frequency
$\gamma(\Psi)$	[–]	Source term accounting for breakage and coalescence
μ_x	[Pa s]	Dynamic viscosity of the continuous phase
$\dot{\xi}_i$	[–]	Velocity vector along the internal coordinate
ρ_x	[kg m^{-3}]	density of the continuous phase
σ	[N m^{-1}]	Interfacial tension of liquid-liquid system
ϕ_y	[m^{3}m^{-3}]	Volume fraction of the dispersed phase (holdup)
ψ	[–]	Bivariate vector for internal and external coordinate
$\omega(d,d')$	[m^{3}s^{-1}]	Coalescence rate
$\lambda(d,d')$	[–]	Coalescence efficiency

Sub- and Superscripts

b	breakage
c	coalescence
char	characteristic
crit	ritical
d′	diameter of drop
i	internal coordinate
R	rotor
r	relative
t	time
x	continuous phase
y	disperse phase
z	space

Abbreviations

AI	Artificial Intelligence
ANN	Artificial Neural Network
CNN	Convolutional Neural Network
CONV	Convolutional Layer
DL	Deep Learning
FC	Fully Connected Layer
FEP	Fluorinated Ethylene-Propylene
FPN	Feature Pyramid Network
LLE	Liquid-Liquid Extraction
ML	Machine Learning
PBE	Population Balance Equation
RCNN	Region-based Convolutional Network
ROI	Region of Interest
RPN	Region Proposal Network
rpm	Revolution per Minute

References

[1] A. Ari, N. Arregui, S. Black, O. Celasun, D. Iakova, A. Mineshima, V. Mylonas, I. Parry, I. Teodoru, K. Zhunussova, *Surging Energy Prices in Europe in the Aftermath of the War: How to Support the Vulnerable and Speed Up the Transition Away from Fossil Fuels*, IMF Working Papers, 2022/152, International Monetary Fund, Washington, DC **2022**.

[2] O. Sandri, S. Holdsworth, J. Hayes, N. Willand, T. Moore, *Energy Res. Social Sci.* **2021**, *79*, 102179. DOI: https://doi.org/10.1016/j.erss.2021.102179

[3] J. L. Humphrey, A. F. Siebert, *Chem. Eng. Prog.* **1992**, *88*, 80–92.

[4] A. Lucia, A. Amale, R. Taylor, *Ind. Eng. Chem. Res.* **2006**, *45 (25)*, 8319–8328. DOI: https://doi.org/10.1021/ie060035t

[5] A. Holbach, S. Soboll, B. Schuur, N. Kockmann, *Ind. Eng. Chem. Res.* **2015**, *54 (33)*, 8266–8276. DOI: https://doi.org/10.1021/acs.iecr.5b00896

[6] J. Kampwerth, D. Roth, L. Polte, A. Jupke, *Ind. Eng. Chem. Res.* **2022**, *61 (9)*, 3374–3382. DOI: https://doi.org/10.1021/acs.iecr.1c03312

[7] M. Agudo, A. Ríos, M. Valcárcel, *Analyst* **1994**, *119 (9)*, 2097–2100. DOI: https://doi.org/10.1039/AN9941902097

[8] J. Ritter, M. Kraume, *Chem. Eng. Technol.* **2000**, *23 (7)*, 579–581. DOI: https://doi.org/10.1002/1521-4125(200007)23:7<579:AID-CEAT579>3.0.CO;2-Y

[9] N. Kockmann, L. Bittorf, W. Krieger, F. Reichmann, M. Schmalenberg, S. Soboll, *Chem. Ing. Tech.* **2018**, *90 (11)*, 1806–1822. DOI: https://doi.org/10.1002/cite.201800020

[10] M. Schmalenberg, F. Sallamon, C. Haas, N. Kockmann, in *Proc. of the ASME 2020 18th International Conference on Nanochannels, Microchannels, and Minichannels collocated with the ASME 2020 Heat Transfer Summer Conference and the ASME 2020 Fluids Engineering Division Summer Meeting*, in press. DOI: https://doi.org/10.1115/ICNMM2020-1062

[11] C. Kröger, V. Khaydarov, L. Urbas, *Comput.-Aided Chem. Eng.* **2022**, *51*, 1363–1368.

[12] V. Uraikul, C. W. Chan, P. Tontiwachwuthikul, *Eng. Appl. Artif. Intell.* **2007**, *20 (2)*, 115–131. DOI: https://doi.org/10.1016/j.engappai.2006.07.002

[13] V. Pandiyan, S. Shevchik, K. Wasmer, S. Castagne, T. Tjahjowidodo, *J. Manuf. Processes* **2020**, *57*, 114–135. DOI: https://doi.org/10.1016/j.jmapro.2020.06.013

[14] P. Wiederkehr, F. Finkeldey, T. Merhofe, *CIRP Ann.* **2021**, *70 (1)*, 297–300. DOI: https://doi.org/10.1016/j.cirp.2021.04.051

[15] M. Bortz, K. Dadhe, A. P. Mitsos, *Chem. Ing. Tech.* **2021**, *93 (12)*, 1875.

[16] J. D. Seader, E. J. Henley, *Separation process principles*, 2nd ed., John Wiley & Sons, Hoboken, NJ **2006**.

[17] S. Soboll, L. Bittorf, N. Kockmann, *Chem. Eng. Technol.* **2018**, *41 (1)*, 134–142. DOI: https://doi.org/10.1002/ceat.201700152

[18] A. S. Behr, L. M. Neuendorf, P. Sakthithasan, K. E. Boettcher, N. Kockmann, in *2022 IEEE German Education Conference (GeCon)*, IEEE, Piscataway, NJ **2022**.

[19] R. Chauhan, K. K. Ghanshala, R. Joshi, in *2018 First International Conference on Secure Cyber Computing and Communication (ICSCCC 2018)*, IEEE, Piscataway, NJ **2018**.

[20] I. Goodfellow, Y. Bengio, A. Courville, *Deep Learning*, MIT Press, Cambridge, MA **2016**.

[21] R. Bobba, *Taming the Hyper-Parameters of Mask RCNN*, Medium Analytics Vidhya, available at https://medium.com/analytics-vidhya/taming-the-hyper-parameters-of-mask-rcnn-3742cb3f0e1b, **2019**.

[22] K. He, G. Gkioxari, P. Dollár, R. Girshick, *Mask R-CNN*, Computer Vision and Pattern Recognition, arXiv:1703.06870, **2017**. DOI: https://doi.org/10.48550/arXiv.1703.06870

[23] R. Girshick, in *2015 IEEE International Conference on Computer Vision (ICCV)*, IEEE, Piscataway, NJ **2015**.

[24] W. Abdulla, *Splash of Color: Instance Segmentation with Mask R-CNN and TensorFlow*, Matterport Engineering Techblog, available at https://github.com/matterport/Mask_RCNN **2018**.

[25] M. M. Attarakih, H.-J. Bart, T. Steinmetz, M. Dietzen, N. M. Faqir, *Open Chem. Eng. J.* **2008**, *2 (1)*, 10–34.

[26] H. Bahmanyar, M. J. Slater, *Chem. Eng. Technol.* **1991**, *14 (2)*, 79–89.

[27] V. Cauwenberg, J. Degrève, M. J. Slater, *Can. J. Chem. Eng.* **1997**, *75 (6)*, 1046–1055.

[28] S. A. Schmidt, M. Simon, H.-J. Bart, *Chem. Ing. Tech.* **2003**, *75 (12)*, 62–68.

[29] M. Simon, *Koaleszenz von Tropfen und Tropfenschwärmen*, Dissertation, TU Kaiserslautern **2004**.

[30] S. A. Schmidt, M. Simon, M. M. Attarakih, G. L. Lagar, H.-J. Bart, *Chem. Eng. Sci.* **2006**, *61 (1)*, 246–256.

[31] D. Garthe, *Fluiddynamics and Mass Transfer of Single Particles and Swarms of Particles in Extraction Columns*, Dissertation, TU München **2006**.

[32] G. L. Lane, M. P. Schwarz, G. M. Evans, *Chem. Eng. Sci.* **2005**, *60*, 2203–2214.
[33] M. Laso, *A model of the dynamic simulation of liquid liquid dispersion*, Doctoral Thesis, ETH Zürich **1986**.
[34] G. Casamatta, A. Vogelpohl, *Chem. Ing. Tech.* **1984**, *56 (3)*, 230–231.
[35] C. A. Coulaloglou, L. L. Tavlarides, *Chem. Eng. Sci.* **1977**, *32 (11)*, 1289–1297.
[36] M. Attarakih, S. Al-Zyod, M. Abu-Khader, H.-J. Bart, *Procedia Eng.* **2012**, *42*, 1445–1462.
[37] C. Drumm, H.-J. Bart, Coupling of CFD with DPBM: Drop Size Distributions and Flow Fields in a RDC Extractor, in *6th Int. Conference on Multiphase Flow* (Eds: M. Sommerfeld, C. Tropea), Leipzig, **2007**.
[38] L. Gomes, M. Guimarães, P. Regueiras, J. Stichlmair, J. Cruz Pinto, *Ind. Eng. Chem. Res.* **2006**, *45 (11)*, 3955–3968.
[39] A. Klee, R. Treybal, *AIChE J.* **1956**, *4*, 444–447.
[40] A. Vignes, *Genie Chim.* **1965**, *93 (5)*, 129–142.
[41] J. Fang, J. C. Godfrey, Z.-Q. Mao, M. J. Slater, C. Gourdon, *Chem. Eng. Technol.* **1995**, *18 (1)*, 41–48.
[42] M. Henschke, *Auslegung pulsierter Siebboden-Extraktionskolonnen*, Postdoctoral Thesis, Shaker Verlag, Aachen **2004**.
[43] J. C. Godfrey, M. J. Slater, *Liquid-Liquid Extraction Equipment.: Rate Coefficients in Liquid-Liquid Extraction Systems*, Wiley, New York **1995**.
[44] S. Soboll, I. Hagemann, N. Kockmann, *Chem. Ing. Tech.* **2017**, *89 (12)*, 1611–1618. DOI: https://doi.org/10.1002/cite.201700031
[45] S. Höving, J. Bobers, N. Kockmann, *J. Flow Chem.* **2022**, *12 (2)*, 185–196. DOI: https://doi.org/10.1007/s41981-021-00214-w
[46] L. M. Neuendorf, F. Z. Baygi, P. Kolloch, N. Kockmann, *ACS Eng. Au* **2022**, *2 (4)*, 369–377. DOI: https://doi.org/10.1021/acsengineeringau.2c00014
[47] D. Kossmann, T. Wilhelm, G. A. Fink, in *2020 25th International Conference on Pattern Recognition (ICPR)*, IEEE, Piscataway, NJ **2020**.
[48] L. Neuendorf, P. Müller, C. Bergeest, A. Meijer, C. C. Schlander, N. Kockmann, Künstliche Intelligenz (KI)-basierte optische Sensorik für flüssig-flüssig Systeme, in *Proc. 16. Dresdner Sensor-Symposium 2022*, AMA Service, Wunstorf **2022**. DOI: https://doi.org/10.5162/16dss2022/P50
[49] S. A. Schmidt, M. Simon, M. M. Attarakih, G. L. Lagar, H.-J. Bart, *Chem. Eng. Sci.* **2006**, *61 (1)*, 246–256.

